3D Printed Flexible PVDF-TrFE Composites with Aligned BCZT Nanowires and Interdigital Electrodes for Piezoelectric Nanogenerator Applications

Mingyang Yan [1†], Huimin Li [1†], Shengwen Liu [1], Zhida Xiao [1], Xi Yuan [2], Di Zhai [1], Kechao Zhou [1], Dou Zhang[1*], Chris Bowen [3], Yan Zhang [1*]

[1] State Key Laboratory of Powder Metallurgy, Central South University, Changsha, Hunan 410083, China.

[2] College of Chemistry and Chemical Engineering, Central South University, Changsha, Hunan 410083, China.

[3] Department of Mechanical Engineering, University of Bath, United Kingdom, Bath, BA27AY, UK

Corresponding Authors

[*] E-mail: dzhang@csu.edu.cn (Dou Zhang); yanzhangcsu@csu.edu.cn (Yan Zhang)

ABSTRACT

Piezoelectric nanogenerators based on piezoelectric nanocomposites have attracted significant interest in recent years due to their excellent piezoelectric properties and potential application in self-powered systems and wearable sensors. As a promising piezoelectric ceramic filler in composite-based generators, one-dimensional (1D) piezoelectric nanowires have been introduced into a polymer matrix to improve the dielectric and piezoelectric properties. In this paper, flexible PVDF-TrFE composite films containing highly aligned $Ba_{0.85}Ca_{0.15}Ti_{0.9}Zr_{0.1}O_3$ (BCZT) nanowires (NWs) have been fabricated using a direct ink writing method. The effect of BCZT nanowire content on the dielectric, ferroelectric and piezoelectric properties was investigated in detail. The piezoelectric energy harvesting figures of merit initially increases, and then begins to decrease, with an increasing content of BCZT nanowires, where a maximum harvesting figure of merit value of 5.3×10^{-12} m^2/N was obtained for a 15 wt% BCZT NWs/PVDF-TrFE composite film. Interdigital electrodes were combined with the composite to fabricate a patterned piezoelectric nanogenerator, where the piezoelectric nanogenerator is shown to generate a maximum output voltage of 17 V, with a peak output power density of 5.6 $\mu W/cm^2$. This work provides new opportunities for the design and manufacture of high-performance piezoelectric composites for piezoelectric energy harvesting and sensing applications.

KEYWORDS: direct ink writing, BCZT nanowires, nanowire alignment, interdigital electrodes, energy harvesting

1. Introduction

The development of 5G technology and smart cities has brought significant benefits with regards to the Internet of Things (IoT) and wireless sensors [1, 2]. In the era of smart cities, smart wireless sensors can play the role of monitoring the whole city in real time due to the ability to detect a range of stimuli, including mechanical loads and temperature signals [3-5]. However, the development of sustainable energy sources and self-powered sensing systems for smart cities represents a primary challenge, which has inspired researchers to develop new technologies for both energy harvesting and sensing. The emergence of piezoelectric nanogenerators has also led to significant interest in this field, since they can convert mechanical vibrations, force, accelerations, and human movements into electrical energy [6-8]. Therefore, piezoelectric nanogenerators can provide sustainable and clean power for wearable sensors of smart cities.

As an important component of a piezoelectric nanogenerator, the piezoelectric materials have been investigated by many researchers in recent few decades. Piezoelectric ceramics, such as lead zirconate titanate (PZT) [9] and barium titanate (BT) [10], have been studied for sensing and energy harvesting applications. However, the inherent brittleness and high relative permittivity of piezoelectric ceramics make them undesirable in sensors, harvesters and wearable electronic devices. Piezoelectric polymers, which are often based on poly(vinylidene fluoride), PVDF, and its copolymers, are also candidate materials but exhibit relatively low piezoelectric coefficients [11, 12]. As a result, piezoelectric nanocomposites, which combine the high

piezoelectric coefficient of ceramics with the mechanical flexibility of piezoelectric polymers, have attracted significant interest in this field. Among these piezoelectric nanocomposites, poly-[(vinylidene fluoride)-co-trifluoroethylene] (PVDF-TrFE) based nanocomposites have been considered as promising candidates for piezoelectric nanogenerators due to its enhanced piezoelectric properties and tunable mechanical properties and flexibility [13-16].

A variety of piezoelectric ceramic fillers have been introduced into a piezoelectric polymer matrix to create piezoelectric nanocomposites, including zero-dimensional (0D) piezoelectric nanoparticles, one-dimensional (1D) piezoelectric nanowires and two-dimensional (2D) piezoelectric nanosheets [17,18]. For example, $BaTiO_3$@Carbon (BT@C) nanoparticles have been introduced into a piezoelectric PVDF-TrFE matrix to fabricate a flexible piezoelectric nanogenerator, and the output voltage was 16 V [19]. Shi *et al.* proposed a flexible piezoelectric nanogenerator that consisted of polymethyl methacrylate (PMMA) encapsulated $BaTiO_3$ nanowires and PVDF-TrFE. The output voltage and current of the piezoelectric nanogenerator were 12.6 V and 1.30 μA, respectively [20]. It is demonstrated that piezoelectric nanocomposites with 1D piezoelectric fillers exhibit a higher polarization and output power density compared to composites based on 0D piezoelectric nanoparticles [21, 22]. For example, Zhou *et al*. demonstrated that the output power density of a nanogenerator based on $0.5Ba(Zr_{0.2}Ti_{0.8})O_3-0.5(Ba_{0.7}Ca_{0.3})TiO_3$ (BCZT) nanowires and poly(dimethylsiloxane) (PDMS) was approximately nine times higher than a nanoparticle-based composite [23]. Moreover, the load transfer efficiency of piezoelectric nanowires-based

composites is higher than that of a piezoelectric nanoparticles-based nanocomposite [24]. As a result, piezoelectric nanowire-based nanocomposites have attracted much attention in recent years due to their piezoelectric and mechanical properties.

For piezoelectric nanocomposites based on 1D nanowires, the degree of alignment of the piezoelectric nanowires has a significant effect on performance [25]. Xie *et al.* investigated the effect of the alignment of the barium titanate nanowires within a piezoelectric P(VDF-CFE) matrix on the dielectric, ferroelectric and energy storage performance; their results showed that aligning the piezoelectric nanowires parallel to the poling direction leads to a higher dielectric constant, remnant polarization and energy density compared to the alignment of piezoelectric nanowires perpendicular to the poling direction [26]. Zhu *et al.* fabricated a piezoelectric nanogenerator based on arrays of vertically aligned ZnO nanowires, which exhibited a maximum power density of 0.78 W/cm^3 [27]. Subsequently, Malakooti *et al.* arranged barium titanate nanowires in a polylactic acid (PLA) solution along three different axes of alignment (0°, 45°, and 90°) via a 3D printing process. The power generation capacity of the nanocomposites with nanowires orientated a 0° was 273% higher compared to nanocomposites with randomly oriented nanowires [28]. The literature therefore demonstrates the potential of piezoelectric nanocomposites based on highly aligned nanowires in piezoelectric nanogenerators. Currently, the fabrication of piezoelectric nanocomposites with aligned nanowires are primarily based on electrospinning [29], hot pressing [30], in situ dielectrophoretic [31] and uniaxial strain assembly [32]. Unfortunately, these fabrication methods have their own limitations, which make them complex and less

versatile for the manufacture of piezoelectric nanocomposites with aligned nanowires. Recently, direct ink writing has been considered as a facile, rapid, and versatile fabrication method for the alignment of piezoelectric nanowires in polymer matrices [33-35]. The shear-induced alignment of direct ink writing is relatively simple and easy to achieve without the application of an external field, and various types of piezoelectric nanocomposites can be fabricated with proper control of processing conditions [36, 37]. For example, Gao *et al.* fabricated a flexible piezoelectric nanogenerator that was composed of $(Na,K)NbO_3$ (KNN) nanowires in a polydimethylsiloxane (PDMS) matrix by a direct ink writing method. The output voltage was nearly 400% higher than a material based on a traditional spin-coated process due to the alignment of nanowires [38]. Despite these developments, research of piezoelectric nanocomposites with an aligned structure fabricated by direct ink writing is still less well developed, and most are based on PDMS. In addition, the device architecture and electrode optimization required further investigation.

Herein, a direct ink writing method was utilized to fabricate a flexible piezoelectric nanogenerator consisting of highly aligned BCZT NWs and a PVDF-TrFE matrix for piezoelectric energy harvesting applications. Interdigital electrodes were designed and optimized to enhance the output performance of the piezoelectric nanogenerator. The effect of BCZT nanowire content on the dielectric, ferroelectric, piezoelectric properties and energy harvesting performance was investigated in detail. The results show that the 15 wt. % BCZT NWs/P(VDF-TrFE) piezoelectric nanogenerator can generate an optimal output voltage of 17 V, with a maximum output power density of 5.6 $\mu W/cm^2$.

This work provides a new strategy to design and fabricate high-performance piezoelectric nanogenerators with highly aligned fillers and expands their application for sensing and energy harvesting.

2. Experimental Section

2.1 Fabrication of $Ba_{0.85}Ca_{0.15}Ti_{0.9}Zr_{0.1}O_3$ (BCZT) nanowires

The $Ba_{0.85}Ca_{0.15}Ti_{0.9}Zr_{0.1}O_3$ (BCZT) NWs were fabricated by using an electrospinning method. All chemicals used were analytical grades. Barium acetate, calcium acetate monohydrate, zirconium acetylacetonate, acetylacetone and tetrabutyl titanate were weighed according to the required molar ratio. Then, they were sequentially added in the mixed solvent of acetic acid and ethylene glycol monomethyl ether and continuously stirred for 6 h at 40 °C to form a homogeneous BCZT sol. Polyvinylpyrrolidone was added to the BCZT sol and stirred for 12 h to obtain an electrospinning precursor solution. The as-spun BCZT nanowires were formed under a voltage of 10 kV, an injection rate of 1.2 ml/h, and a pinhead-to-collector distance of 15 cm. Finally, high aspect ratio BCZT nanowires were formed after being sintered at 800 °C for 2 h.

2.2 Preparation of piezoelectric composites films

The piezoelectric composites films with aligned BCZT NWs were fabricated via a direct ink writing method. Firstly, BCZT NWs were added to the mixed solvent of dimethylsulfoxide and acetone (3:2) and sonicated at room temperature for 1 h to make them dispersed uniformly in the solution. Then, PVDF-TrFE powder was added and stirred for 12 h at 40 °C to form a homogeneous solution. The solution was concentrated

by evaporating the solvent of acetone to obtain high viscosity for the printing process. The solution was then transferred to an extrusion syringe with a nozzle of 260 μm diameter and the composite films with the mass fraction of 5, 10, 15 and 20 BCZT nanowires were printed onto the glass substrate. Finally, these composite films were dried at 70 °C for 24 h in the vacuum oven to evaporate the residual solvent.

2.3 Fabrication of the flexible piezoelectric nanogenerator

The fabricated PVDF-TrFE composite films with BCZT nanowire with a loading content of 15 wt% were cut into rectangular pieces with dimensions of 1.5 × 3 cm^2. Then, gold interdigital electrodes were deposited on the top and bottom sides of the composite film by magnetic sputtering. Silver wires were pasted on the electrodes by silver epoxy, and polyimide films were used to package the composite films to protect them from harmful environment. Finally, the packaged composite films were polarized under an electric field of 10 kV/mm at 60 °C in an oil bath for 8 h.

2.4 Finite element simulation analysis

COMSOL Multiphysics 5.4 (combinations of Solid Mechanics, Electrostatics, and Electrical Circuit Modules) was used to evaluate the distribution of the piezoelectric potential and electric field in the PVDF-TrFE composite films with aligned and randomly distributed BCZT NWs. Two two-dimensional models with dimension of 72 × 72 μm were created, and the diameter of the BCZT nanowires was 300 nm. A load of 20 N was applied to the upper surface with the lower set to ground (0V) to investigate the piezoelectric potential distribution of the composite films. Moreover, an electric field of 30 kV/mm was applied to explore the electric field distribution within the

composite films.

2.5 Characterization and measurements

The morphology of BCZT NWs and PVDF-TrFE composite films was examined by field emission scanning electron microscopy (FESEM, NovaNanoSEM230, USA). High-resolution transmission microscopy (HRTEM Titan G260-300) was used to analyze the microstructure of BCZT NWs. The crystal structure of BCZT NWs and PVDF-TrFE composite films were evaluated by X-ray diffraction (XRD) using Cu Kα radiation. The BCZT NWs were examined by X-ray photoelectron spectroscopy (XPS, ThermoFisher Scientific Escalab250Xi), and the chemical structure and functional group of the PVDF-TrFE composite films for different loading contents of BCZT NWs were characterized by Fourier-transform infrared spectroscopy (FT-IR, VERTEX 70 V). The rheological properties of ink were tested by Rheometer (AR 2000EX, TA Instruments). The dielectric constant and dielectric loss of the composite films were measured using a Precision Impedance Analyzer (4294A; Agilent Technologies, Santa Clara, USA). The polarization-electric field (P-E) loops were characterized by a TF Analyzer 3000 (AixACCT systems, Germany). The piezoelectric charge coefficient d_{33} was measured using a piezoelectric d_{33} meter (ZJ-4AN, Institute of Acoustics, Academic Sinica, China), and the piezoelectric output of the PVDF-TrFE composite film with 15 wt% BCZT NWs was evaluated in detail. A periodic compressive stress at a specific frequency of 2 Hz was applied through a linear motor. The output voltage and current of the flexible piezoelectric nanogenerator were measured by a Keithley 6517B electrometer.

3. Results and discussion

Fig. 1a shows the fabrication process to create piezoelectric composite films with highly aligned BCZT nanowires and a flexible piezoelectric nanogenerator with interdigital electrodes; detailed information has been provided in the Experimental Section. Firstly, BCZT NWs were synthesized by an electrospinning method, as shown in **Fig. 1**a (i) and (ii). Then, the BCZT NWs were dispersed into a mixed solvent of dimethyl sulfoxide (DMSO) and acetone, followed by the addition of PVDF-TrFE powder to the solution to form an ink for direct ink writing, as shown in **Fig. 1**a (iii). The prepared ink was transferred to a syringe and extruded through a micronozzle onto the glass substrate, and the BCZT NWs were aligned by the shear force during this process, as shown in **Fig. 1**a (iv). After evaporation of the solvent, the PVDF-TrFE composite films with different loading contents of BCZT NWs were peeled from the substrate. Finally, interdigital electrodes were deposited on the top and bottom sides of the film, as shown in **Fig. 1**a (vi). A schematic of the flexible piezoelectric nanogenerator is presented in **Fig. 1**b. It can be seen from **Fig. 1**c and **Fig. 1**d that the printed film with interdigital electrodes (IDE) possessed good flexibility. Two conductive wires were connected to the IDE electrodes and polyimide films were used to package the composite film to form the flexible piezoelectric nanogenerator, as shown in **Fig. 1**d.

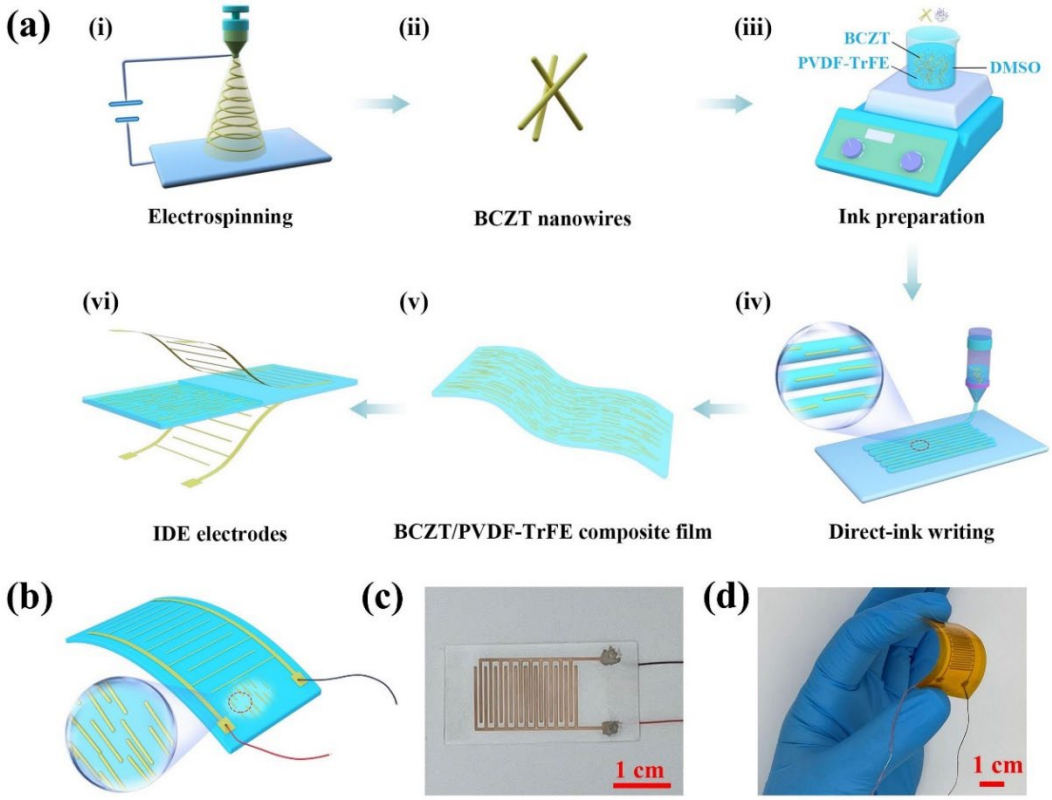

Fig. 1 (a) Schematic for the fabrication process of the flexible piezoelectric nanogenerator. (b) Schematic configuration of the flexible piezoelectric nanogenerator. Photographs of (c) PVDF-TrFE composite film with 15 wt% BCZT nanowires (NWs) and (d) flexible piezoelectric nanogenerator.

Scanning electron microscopy (SEM) images of the BCZT NWs before and after sintering are presented in **Fig. 2**a-b. It can be observed that the as-spun BCZT NWs are smooth and continuous, without any pores or beads. After sintering, the BCZT NWs become discontinuous and the surface is relatively rough due to the volatilization and decomposition of organic solvent. High resolution transmission electron microscopy (HRTEM) was performed to further investigate crystalline structures and physical properties of the BCZT NWs. The HRTEM images demonstrate that the BCZT NWs have a polycrystalline structure, as indicated in **Fig. 2**d, the crystal plane spacing is

0.282 nm, which corresponds to the (110) crystal planes of XRD results [39]. Energy Dispersive Spectroscopy (EDS) mapping analysis of the BCZT NWs is shown in **Fig. 2**e. It can be seen that all elements related to Ba, Ca, Zr, Ti, and O are collected by EDS, and these elements are homogeneously distributed in mapping images, indicating the successful synthesis of BCZT NWs.

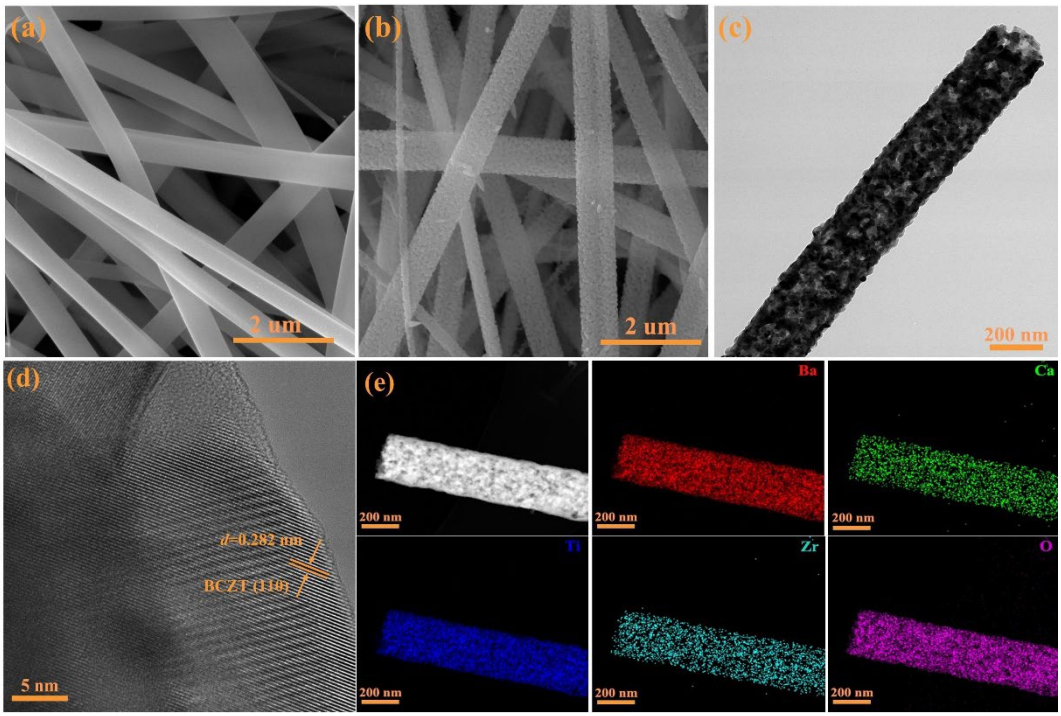

Fig. 2 SEM images of the BCZT NWs (a) before sintering. (b) after sintering. (c-d) HRTEM images. (e) EDS mapping of the BCZT NWs.

Fig. 3a shows the XRD pattern of the BCZT NWs, where it can be observed that all peaks can be indexed with pure perovskite phase, without any second phase. It can be observed from the inset of **Fig. 3**a that there is a small splitting of the (200) peak. For $BaTiO_3$-based piezoelectric ceramics, splitting of the (200) peak is related to the existence of a tetragonal phase [40]. In order to conform the chemical states of the elements of BCZT NWs, XPS measurements were conducted, where it can be observed

from **Fig. 3**b that all the peaks that belong to Ba 3d, Ca 2p, Zr 3d, Ti 2p, and O 1s are detected in BCZT NWs. **Fig. 3**c and **Fig. 3**d show fitting curves of Ba 3d and Ti 2p peaks, where peak splitting is attributed to the co-occupancy of Ba^{2+} and Ca^{2+} in the A site and Zr^{4+} and Ti^{4+} in the B site [41]. The Raman spectrum of BCZT NWs is presented in **Fig. 3**e, where three main peaks can be observed in the spectrum; the peak of E, B_1(TO + LO) modes appear at approximately 300 cm^{-1} and demonstrate the existence of the tetragonal phase in the lattice. The peak at approximately 520 cm^{-1} represents the vibration of the TO_6 octahedron, and the peak at approximately 723 cm^{-1} is related to the $A_1(LO_3)$/$E(LO_3)$ modes [42]. To further investigate the piezoelectric properties of BCZT NWs, piezoresponse force microscopy (PFM) was performed to explore the local piezoelectric response. As shown in **Fig. 3**f, the typical amplitude voltage butterfly loops and well-defined piezo-response phase reversal hysteresis loops can be observed, demonstrating the excellent piezoelectric features of the BCZT nanowires.

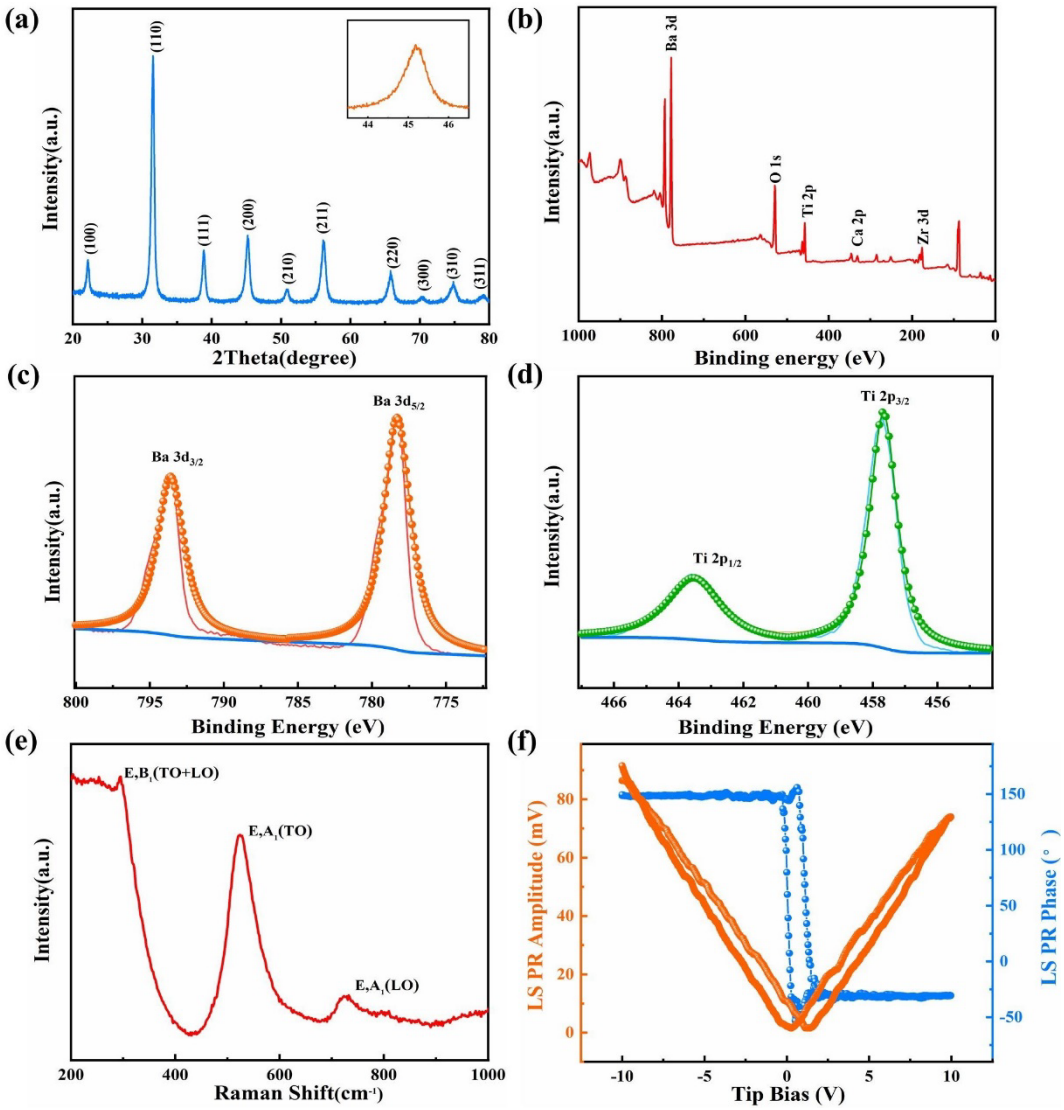

Fig. 3 (a) XRD pattern of BCZT nanowires (NWs). (b) XPS spectrum. (c) XPS spectra of Ba 3d. (d) XPS spectra of Ti 2p. (e) Raman spectroscopy of BCZT NWs. (f) piezoelectric response force microscopy (PFM) hysteresis loop (phase) and butterfly loop (amplitude) of BCZT NWs.

Since BCZT NWs/PVDF-TrFE composite films were fabricated by a direct ink writing method, therefore, the rheological properties are very important. **Fig. S**1 shows the relationship between shear rate and viscosity of PVDF-TrFE ink with different weight contents of BCZT NWs. It can be seen that the viscosity of all the PVDF-TrFE

inks decreases with increasing shear rate, thereby exhibiting a shear thinning behavior, which is highly suitable for a direct ink writing process. The viscosity increases with an increasing load content of BCZT NWs, and could reach approximately 30 Pa·s at a shear rate of 0.1 s^{-1} when the loading content of BCZT NWs was 20 wt%. Moreover, the inks show a high viscosity at a low shear rate, which is beneficial for avoiding agglomeration of BCZT NWs in the printing needle tube. The viscosity is low at a high shear rate, which allows the composite inks to be extruded during the printing process. The cross-sectional morphology of the BCZT NWs/PVDF-TrFE composite films are shown in **Fig. 4**. It can be observed that the BCZT NWs are homogenously dispersed in the PVDF-TrFE matrix and exhibit a preferred orientation along the direct writing direction when the content of BCZT NWs is 5 wt.%. With an increasing content of BCZT NWs, the alignment of BCZT NWs becomes clearer, and the composite film with 15 wt.% BCZT NWs content exhibits the best alignment. However, when the nanowire content reaches 20 wt.%, the degree of alignment of BCZT NWs reduces, and the nanowires tend to be randomly distributed in the matrix. This is because the BCZT NWs cannot be dispersed uniformly and are easy to agglomerate at higher contents. The surface morphologies of the PVDF-TrFE composite films are presented in **Fig. S**2. It can be seen that the BCZT NWs were uniformly distributed in the PVDF-TrFE matrix when the loading content was lower than 15 wt.%. However, the BCZT NWs began to agglomerate in the matrix when the loading content was 20 wt.%. Therefore, the addition of BCZT NWs with 15 wt.% less to composite films with the most aligned nanowires.

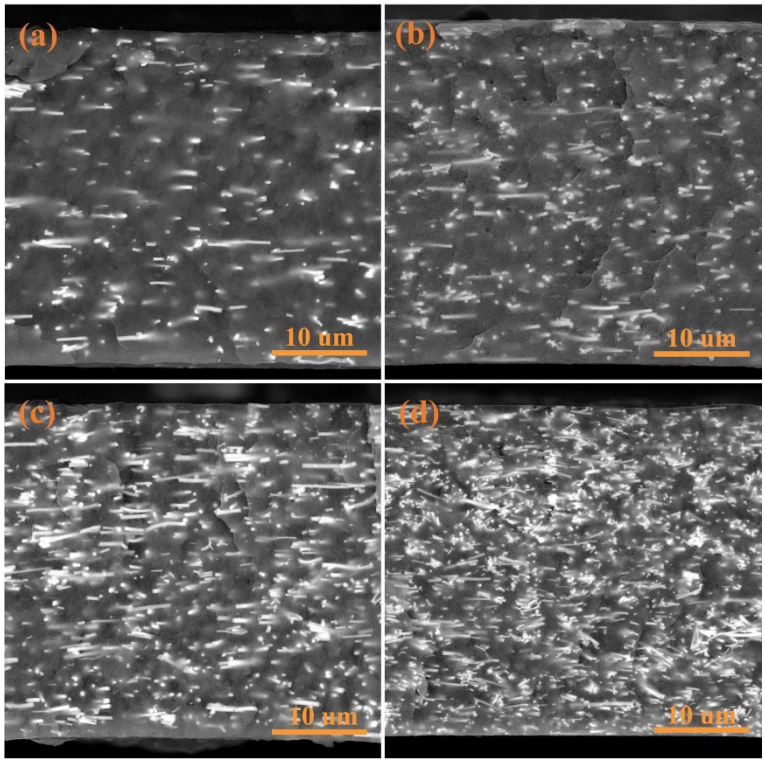

Fig. 4 Cross-sectional SEM images of PVDF-TrFE composite films with different BCZT NWs contents. (a) 5 wt.%. (b) 10 wt.%. (c) 15 wt.%. (d) 20 wt.%.

The XRD spectrum of the pure PVDF-TrFE film and BCZT NWs/PVDF-TrFE composite films with characteristic diffraction peaks at 2θ range from 10° to 70° is presented in **Fig. 5**a. The sharp diffraction peak appears at 2θ = 19.8° represents the reflections of the (110) and (200) orientation planes, which correspond to the polar β-phase of the PVDF-TrFE film [43]. The diffraction peaks of BCZT NWs can be indexed in the composite films without any impurity phases, indicating the existence of BCZT NWs in the films. Moreover, the intensities of the peaks become stronger and the peak intensity of PVDF-TrFE decreases with increasing content of BCZT NWs, which may be attributed to the shielding effect from the high intensity of the diffraction peaks from the BCZT NWs [44]. FITR analysis was performed to further investigate the effect of BCZT NWs content on the β-phase crystallinity of the composite films. As shown in

Fig. 5b, the characteristic peak at 766 cm^{-1} represents the non-polar α-phase, and the characteristic peaks of the typical vibration characteristics of the polar β-phase appear at 843 cm^{-1} and 1276 cm^{-1} according to previous reports [45]. The fraction the polar β-phase can be calculated by the following equation, assuming that the infrared transmittance follows the Lambert−Beer Law:

$$F(\beta) = \frac{A_\beta}{A_\beta + (\frac{k_\beta}{k_\alpha})A_\alpha} \quad (1)$$

Where A_α and A_β represent the absorption peaks at 766 cm^{-1} and 843 cm^{-1}, and K_α = 6.1 × 10^4 cm^2mol^{-1}, K_β = 7.7 × 10^4 cm^2mol^{-1}, respectively. It can be seen from **Fig. 5**c that the fraction of β-phase increases with an increasing content of BCZT NWs and reached a maximum value of 84.3% for composite film with 10 wt.%, indicating the positive effect of BCZT NWs on the piezoelectric activity. The dielectric properties as a function of frequency for the composite films with various BCZT NW contents are shown in **Fig. 5**d and **Fig. 5**e. For all the composite films, the dielectric constant decreases with an increase of frequency, and the dielectric loss initially increases with frequency and then begins to decrease at high frequency due to relaxation of the PVDF-TrFE dipole polarization [46]. A comparison of dielectric constant and loss at 1 kHz for the composite films is presented in **Fig. 5**f, where the dielectric constant increases with an increasing content of nanowire filler, which can be attributed to the large dielectric constant of BCZT. As the content of BCZT NWs increases, the dielectric loss increases slightly due to the formation of conductive pathway induced by the increasing content of BCZT NWs.

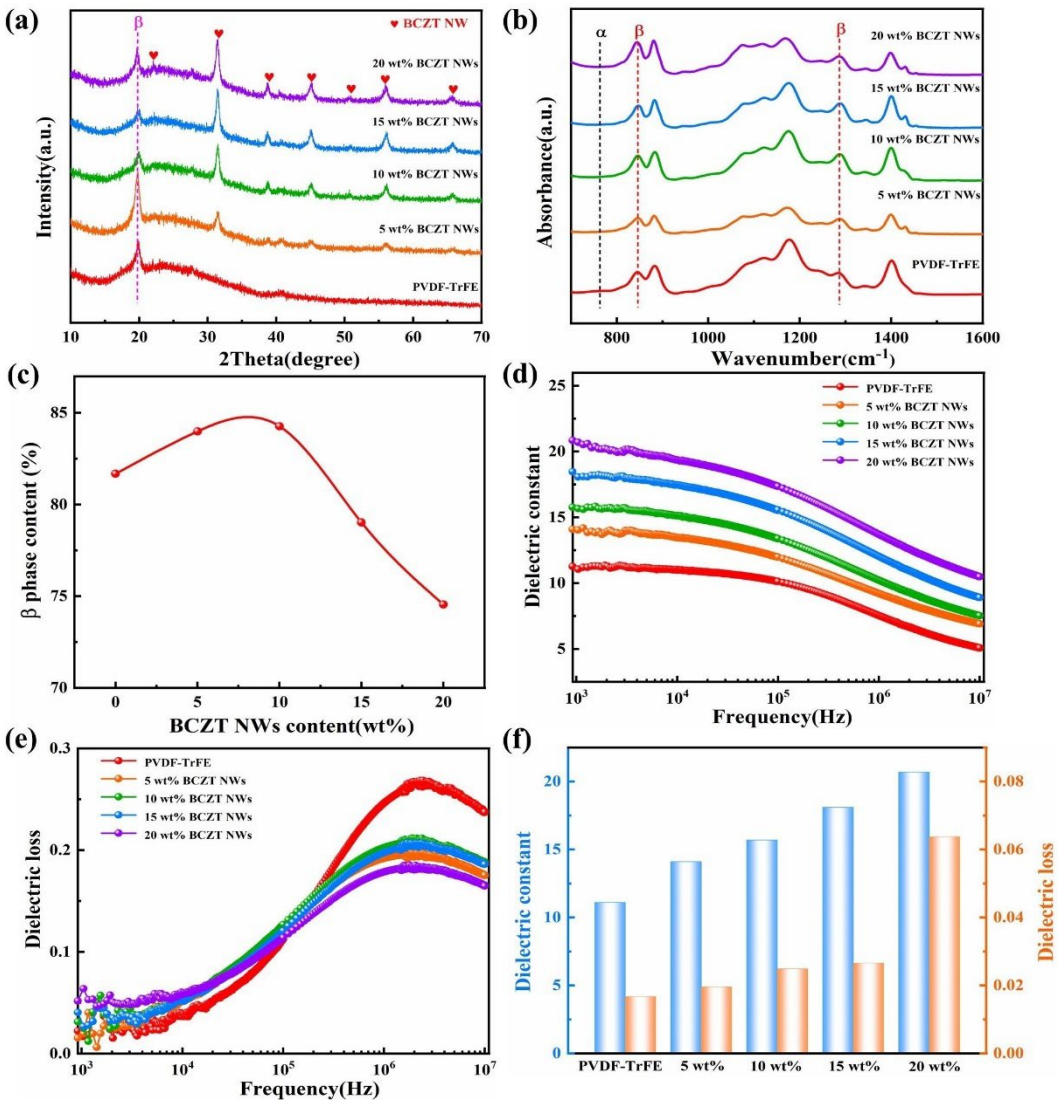

Fig. 5 (a) XRD pattern of the composite films. (b) FITR results of the composite films. (c) calculated results of β phase fraction in the composite films. (d) dielectric constant. (e) dielectric loss. (f) comparison of dielectric constant and loss at 1 kHz.

Typical ferroelectric hysteresis loops of PVDF-TrFE composite films with different loading content of BCZT NWs measured under an electric field of 150 kV/mm are shown in **Fig. 6**a. It can be observed that the shape of hysteresis loops for the composite films with various content of BCZT NWs was symmetrical, demonstrating a good ferroelectric response and domain switching [47]. As shown in **Fig. 6**b, the

remnant polarization (P_r) increases from 2.61 to 9.93 μC cm^{-2} when the content of BCZT NWs increases from 0 to 20 wt.%. Moreover, it can be seen from **Fig. 6**c that the rectangularity (P_r / P_s) increases significantly with the addition of BCZT NWs compared with pure PVDF-TrFE film, which can be attributed to the excellent ferroelectric properties of the BCZT phase. The coercive field (E_c) decreases from 68.2 to 48.1 kV mm^{-1} when the BCZT NW content increases from 0 to 15 wt.%, and increases slightly with a further increase in BCZT NW content. It can be concluded that the addition of BCZT NWs is beneficial in enhancing the ferroelectric polarization and reducing the coercive field of the PVDF-TrFE composite films. In addition, the breakdown strength also plays an important role on the properties of ferroelectric composites. As shown in **Fig. 6**d, the breakdown strength of composite is 173.1, 168.2, 164.7 and 150.1 kV/mm for BCZT NWs contents of 5, 10, 15 and 20 wt.%, respectively. It can be observed that the breakdown strength decreases due to the addition of BCZT NWs, while it decreases more significantly when the content of nanowires reaches 20 wt.% compared to the composite film with 15 wt.% BCZT NWs. It can be concluded that a high loading content of BCZT NWs leads to the formation of a conductive pathway, therefore, the breakdown strength of ferroelectric composites decreases [48]. The piezoelectric properties of the composite films are also evaluated, where it can be seen from **Fig. 6**e that the piezoelectric coefficient increases and then begins to decrease with an increasing content of BCZT NWs. The maximum piezoelectric coefficient of 30 pC/N is obtained when the content of BCZT NWs is 15 wt.%. Furthermore, the piezoelectric voltage coefficient ($g_{33} = d_{33}/\varepsilon_{33}^{T}\varepsilon_0$) and the piezoelectric energy harvesting

figure of merits ($FoM_{33} = d_{33}^2/\varepsilon_{33}^T \varepsilon_0$) are also shown in **Fig. 6**f. It can be observed that the composite film with 15 wt.% BCZT NWs possesses the highest harvesting FoM_{33}, which is 93.4% higher than that of the pure PVDF-TrFE film. Therefore, the composite film with 15 wt.% BCZT NWs are more suitable for energy harvesting applications.

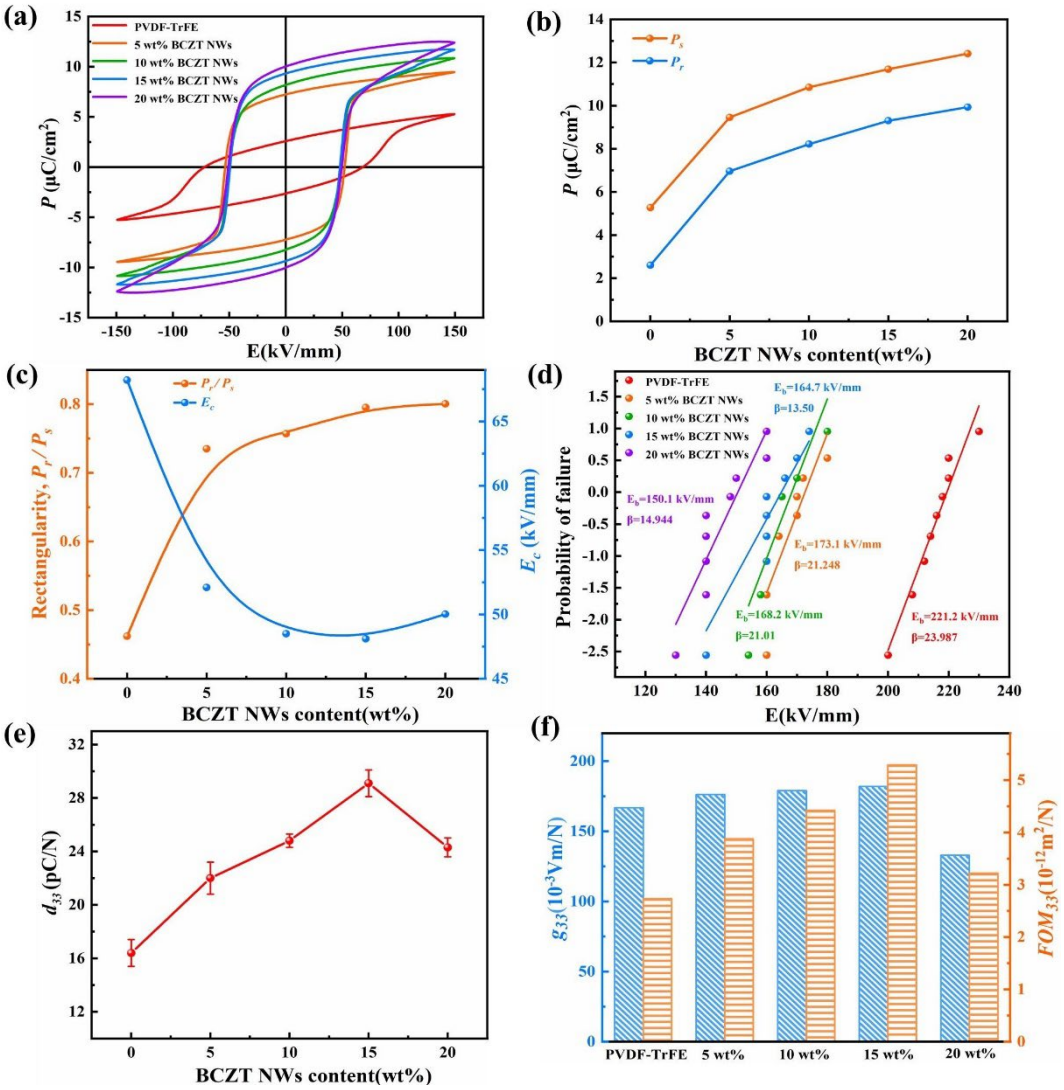

Fig. 6 (a) Ferroelectric hysteresis loops. (b) Spontaneous polarization (P_s) and remnant polarization (P_r). (c) coercive field and rectangularity. (d) breakdown strength. (e) piezoelectric coefficient (d_{33}). (f) piezoelectric voltage coefficient (g_{33}) and piezoelectric energy harvesting figure of merit (FOM_{33}).

PVDF-TrFE composite films with 15 wt.% BCZT NWs were selected to evaluate the piezoelectric energy harvesting performance. Gold interdigital electrodes were deposited on the both sides of the film by magnetron sputtering, and polyimide (PI) films were used to encapsulate the composite film to form a flexible piezoelectric nanogenerator. The open circuit voltage of the piezoelectric nanogenerator under a range of mechanical loads (30 – 180 kPa) is presented in **Fig. 7**a and **Fig. 7**b. It can be seen that the output voltage increases from 9.9 to 17 V when the applied pressure increases from 30 to 180 kPa. Moreover, the output voltage exhibits almost a linear relationship with increasing pressure. As shown in **Fig. S**3, the short circuit current is approximately 0.7 μA for an applied pressure of 180 kPa. The output voltage and power as a function of load resistance ranging from 100 kΩ to 1 GΩ are shown in **Figure 7**c. The output voltage increases with increasing load resistance, while the output power increases first, and then begins to decrease with increasing load resistance. The maximum output power density of 5.6 $\mu W/cm^2$ was obtained with a load resistance of 20 MΩ, and corresponds to an impedance matching condition between the piezoelectric device and the electrical load. For practical applications in real-life situation, the stability and durability of the flexible piezoelectric nanogenerator is important. Therefore, a cyclic tapping test was conducted to evaluate the stability and durability of the piezoelectric nanogenerator. As shown in **Fig. 7**d, the output voltage remains almost unchanged after 5000 cycles, demonstrating the excellent mechanical stability of the material and device. A piezoelectric nanogenerator with BCZT NWs randomly distributed in the PVDF-TrFE matrix was fabricated via a facile tape casting method to

make a comparison with the sample fabricated by a direct ink writing method. It can be seen from **Fig. S**4 that the output voltage could reach 4.4 V under the pressure of 180 kPa. The voltage generated by the composite film with aligned BCZT NWs could reach 17 V, which is 2.7 times higher than that of the composite film with randomly distributed BCZT NWs. These results confirm the excellent piezoelectric energy harvesting performance of PVDF-TrFE composite films with aligned piezoelectric nanowires fabricated by direct ink writing.

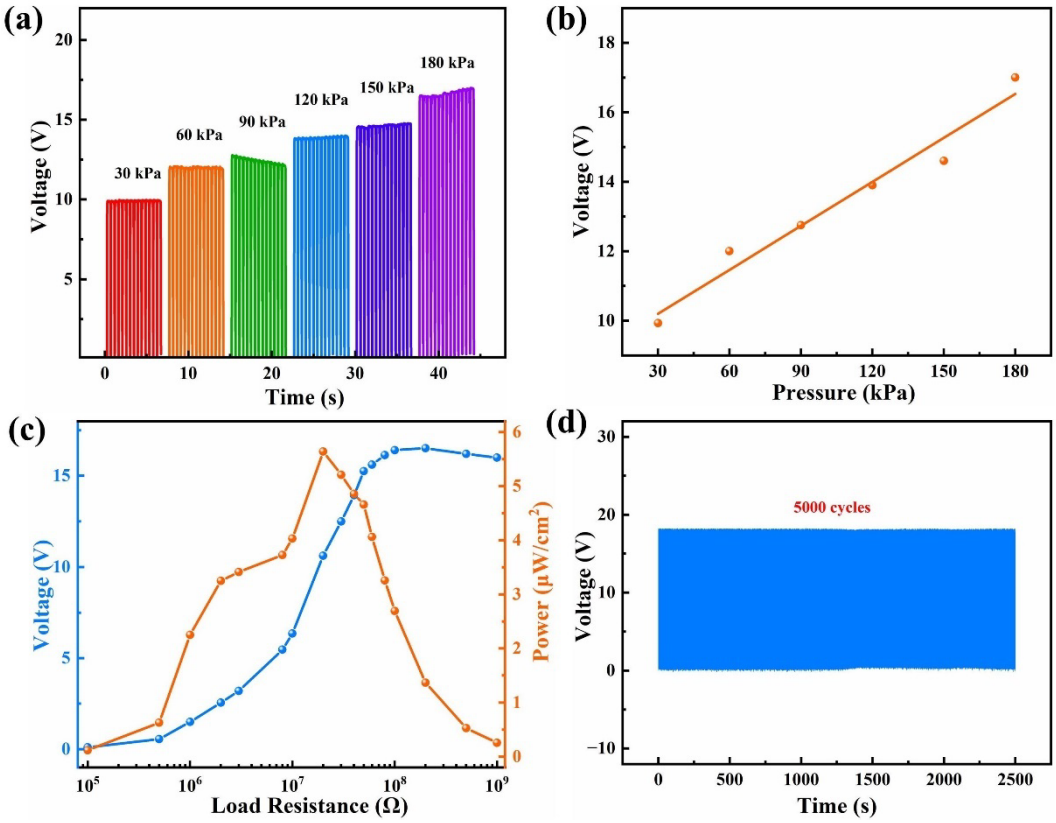

Fig. 7 (a) Open-circuit voltage generated by the piezoelectric nanogenerator. (b) Output voltage as a function of pressure. (c) Output voltage and power with various load resistances. (d) Reliability test of the piezoelectric nanogenerator within 5000 cycles.

Finite element analysis was performed by COMSOL 5.4 software to further explore the output performance enhancement of PVDF-TrFE composite film with

aligned BCZT NWs. The electric field and piezoelectric potential distributions in the composite films with aligned and randomly distributed BCZT NWs were simulated based on two two-dimensional models. The applied electric field and mechanical load was 30 kV/mm and 20 N, respectively. It can be seen from **Fig. 8**a-b, the maximum electric field in the PVDF-TrFE polymer matrix was 9.83×10^8 V/m and 8.67×10^8 V/m for composite films with the aligned and randomly distributed BCZT NWs, respectively. Moreover, the magnitude of the electric field in aligned BCZT NW composite is three times higher than that of randomly distributed BCZT NWs, demonstrating that aligned BCZT NWs can be polarized to a greater extent compared with randomly distributed BCZT NWs. As shown in **Fig. 8**c-d, the piezoelectric potential of the composite film with aligned BCZT NWs is higher than that with randomly distributed BCZT NWs, which is due to the higher stress transfer efficiency of the aligned structure [49]. Therefore, the excellent output performance of the composite film with aligned BCZT NWs can be attributed to the more complete polarization and higher degree of stress transfer.

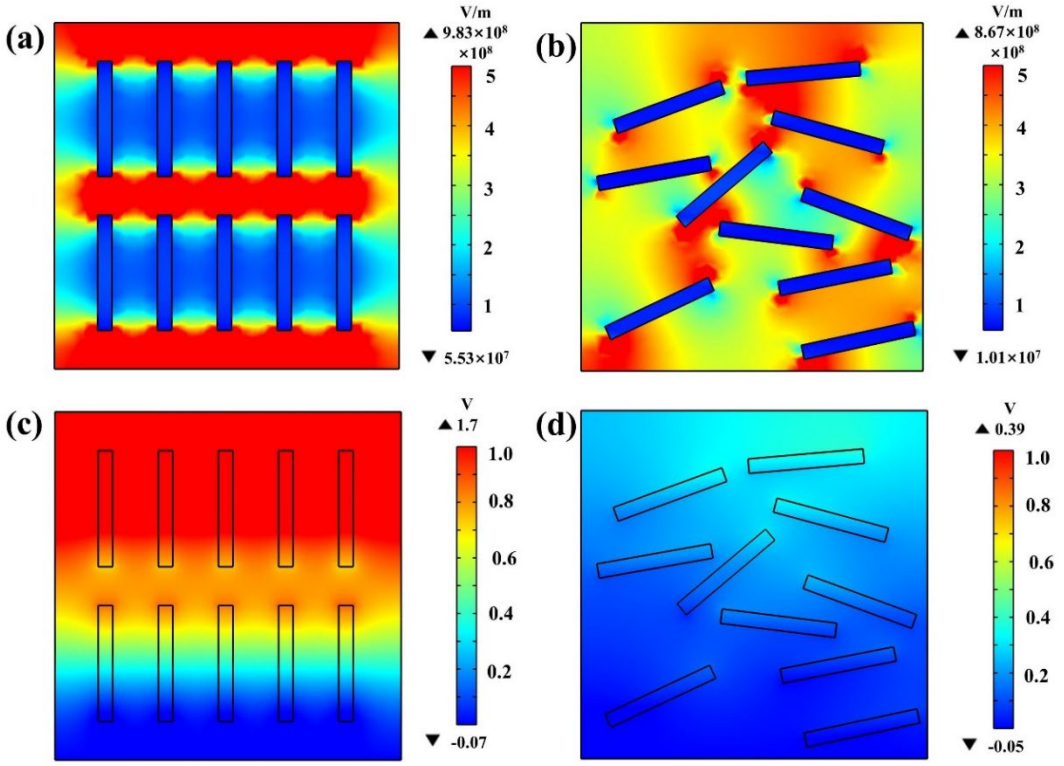

Fig. 8 Electric field distribution of (a) PVDF-TrFE composite film with aligned BCZT NWs. (b) PVDF-TrFE composite film with randomly distributed BCZT NWs. Piezoelectric potential of (c) PVDF-TrFE composite film with aligned BCZT NWs. (d) PVDF-TrFE composite film with randomly distributed BCZT NWs.

A piezoelectric nanogenerator can harvest mechanical energy from our living ambient, for example, harvesting energy from human body movements. Therefore, several scenarios have been designed to explore the potential applications of the flexible piezoelectric nanogenerator in real-life situations. As shown in **Fig. 9**a, the piezoelectric nanogenerator can generate an output voltage of ~ 3.1 V under human finger pressing. It can be seen from **Fig. 9**b and **Fig. 9**c that an output voltage of ~ 6.5 V and 7.7 V can be generated under impact from a human fist and foot, respectively. Moreover, the flexible piezoelectric nanogenerator can be attached to human elbow to produce an output voltage of ~ 12.2 V during elbow bending, as shown in **Fig. 9**d. These results

demonstrate that the flexible piezoelectric nanogenerator can harvest mechanical energy in real life scenarios.

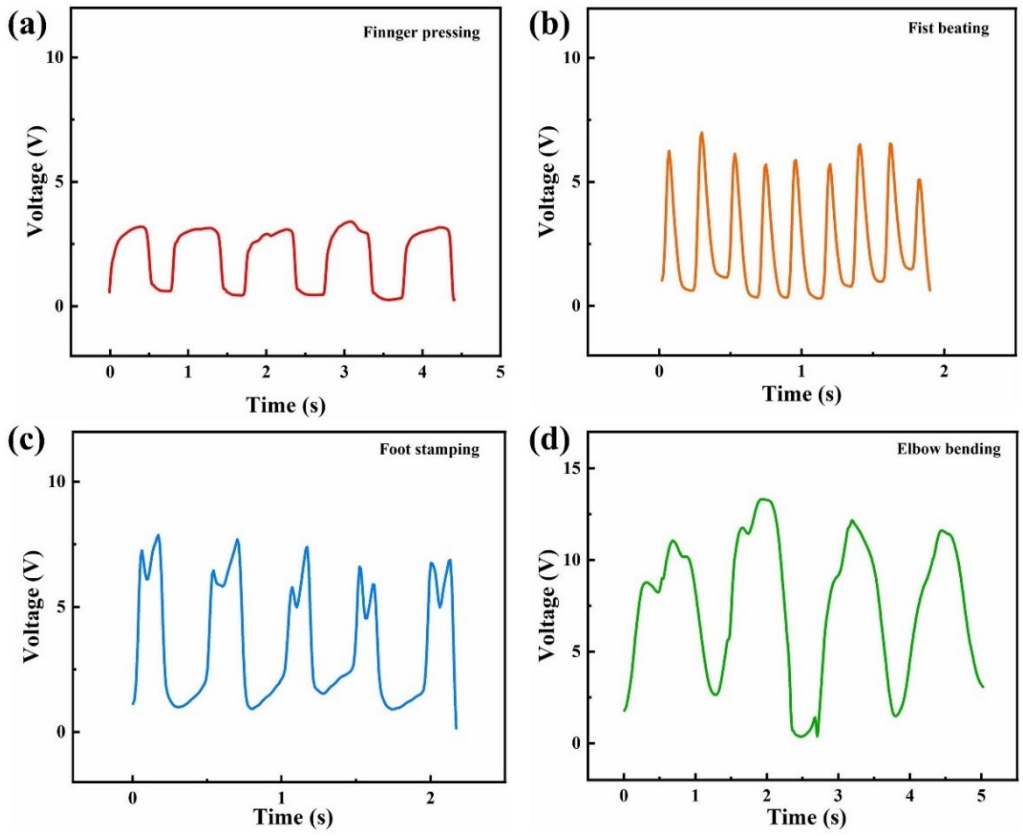

Fig. 9 (a) Output voltage response by light finger pressing. (b) Output voltage response by fist beating. (c) Output voltage response by foot stamping. (d) Output voltage response elbow bending.

4. Conclusion

This paper has developed a novel flexible and high performance piezoelectric nanogenerator that is based on PVDF-TrFE composite films containing highly aligned $Ba_{0.85}Ca_{0.15}Ti_{0.9}Zr_{0.1}O_3$ (BCZT) nanowires and interdigital electrodes. The PVDF-TrFE composite films containing aligned BCZT NWs were fabricated via a facile direct ink writing method, and gold interdigital electrodes were deposited on the film to fabricate

a flexible piezoelectric nanogenerator. The effect of BCZT nanowire content on the dielectric, ferroelectric and piezoelectric properties was investigated in detail. With an increase in BCZT nanowire content, the piezoelectric coefficient initially increases and then begins to decrease. A maximum piezoelectric coefficient was achieved in a 15 wt% BCZT NWs/PVDF-TrFE composite film, which also possess a high piezoelectric energy harvesting figure of merit of 5.3×10^{-12} m^2/N. The piezoelectric energy harvesting performance of the flexible piezoelectric nanogenerator with 15 wt.% BCZT NWs was also evaluated, where the output voltage generated by the sample could reach 17 V, which is 2.7 times higher than that of PVDF-TrFE composite film with randomly distributed BCZT NWs, with the maximum output power of 5.6 $\mu W/cm^2$. Multi-physics modelling demonstrated that controlling the alignment of BCZT NWs in the polymer matrix can increase the effective electric field in composite and nanowires during the poling process, leading to a more complete polarization and improved piezoelectric properties. Therefore, the piezoelectric energy harvesting performance can be enhanced. Moreover, the flexible piezoelectric nanogenerator is demonstrated to have the ability to harvest mechanical energy from human body movements in real-life situations. This work thereby opens a new path for the fabrication of high performance lead-free piezoelectric nanogenerator by controlling the alignment of piezoelectric nanowires in the polymer matrix and introducing interdigital electrodes.

Author Contributions

Mingyang Yan: Conceptualization, Experiment, Investigation, Writing - original draft.

Huimin Li: Conceptualization, Experiment, Investigation. Shengwen Liu: Experiment, Investigation. Zhida Xiao: Investigation, Software. Xi Yuan: Conceptualization, Supervision. Di Zhai: Finite Element Analysis. Kechao Zhou: Conceptualization, Supervision. Dou Zhang: Writing - review & editing. Chris Bowen: Writing - review & editing. Yan Zhang: Supervision, Conceptualization, Writing - review & editing.

ACKNOWLEDGEMENTS

The authors acknowledge the National Key Research and Development Program (2022YFB3807404) and the National Natural Science Foundation of China (No.52172134, 52204263), Key Research and Development Project of Hunan Province (No. 2020WK2004), Overseas Talent Introduction Project of China, Hundred Youth Talents Program of Hunan and State Key Laboratory of Powder Metallurgy, Central South University, Changsha, China. Also, this work was supported by the Fundamental Research Funds for the Central Universities of Central South University.

Declaration of Competing Interest

The authors declare that they have no known competing financial interests or personal relationships that could have appeared to influence the work reported in this paper.

References

1. X. Zhao, H. Askari, J. Chen. Nanogenerators for smart cities in the era of 5g and internet of things. Joule. **5**(6), 1391-1431 (2021). https://doi.org/10.1016/j.joule.2021.03.013

2. T. Wu, Y. Song, Z. Shi, D. Liu, S. Chen, C. Xiong, Q. Yang. High-performance nanogenerators based on flexible cellulose nanofibril/MoS_2 nanosheet composite piezoelectric films for energy harvesting. Nano Energy. **80**, 105541 (2021). https://doi.org/10.1016/j.nanoen.2020.105541

3. A. Alagumalai, O. Mahian, M. Aghbashlo, M. Tabatabaei, S. Wongwises, Z. L. Wang. Towards smart cities powered by nanogenerators: Bibliometric and machine learning–based analysis. Nano Energy. **83**, 105844 (2021). https://doi.org/10.1016/j.nanoen.2021.105844

4. B. Fang, Z. Xin, D. Sun, Z. Li, W. Zhou. Hollow semiconductor photocatalysts for solar energy conversion. Adv Powder Mater. **1**, 100021 (2022). https://doi.org/10.1016/j.apmate.2021.11.008

5. H. L. Wang, Z. H. Guo, X. Pu, Z. L. Wang. Ultralight iontronic triboelectric mechanoreceptor with high specific outputs for epidermal electronics. Nano-Micro Lett. **14**(1), 86 (2022). https://doi.org/10.1007/s40820-022-00834-4

6. Y. Hong, B. Wang, Z. Long, Z. Zhang, Q. Pan, S. Liu, X. Luo, Z. Yang. Hierarchically interconnected piezoceramic textile with a balanced performance in piezoelectricity, flexibility, toughness, and air permeability. Adv Funct Mater. **31**(42), 2104737 (2021). https://doi.org/10.1002/adfm.202104737

7. A. A. Khan, G. Huang, M. M. Rana, N. Mei, M. Biondi, S. Rassel, N. Tanguy, B. Sun, Z. Leonenko, N. Yan, C. Wang, S. Xu, D. Ban. Superior transverse piezoelectricity in organic-inorganic hybrid perovskite nanorods for mechanical energy harvesting. Nano Energy. **86**, 106039 (2021). https://doi.org/10.1016/j.nanoen.2021.106039

8. L. Zhou, L. Zhu, T. Yang, X. Hou, Z. Du, S. Cao, H. Wang, K.-C. Chou, Z. L. Wang. Ultra-stable and durable piezoelectric nanogenerator with all-weather service capability based on n doped 4H-SiC nanohole arrays. Nano-Micro Letters. **14**(1), (2021). https://doi.org/10.1007/s40820-021-00779-0

9. K. Zhang, S. Wang, Y. Yang. A one-structure-based piezo-tribo-pyro-photoelectric effects coupled nanogenerator for simultaneously scavenging mechanical, thermal, and solar energies. Adv Energy Mater. **7**(6), 105844 (2016). https://doi.org/10.1002/aenm.201601852

10. R. S. Sabry, A. D. Hussein. Pvdf: ZnO/$BaTiO_3$ as high out-put piezoelectric nanogenerator. Polym Test. **79**, 106001 (2019). https://doi.org/10.1016/j.polymertesting.2019.106001

11. L. Lu, W. Ding, J. Liu, B. Yang. Flexible pvdf based piezoelectric nanogenerators. Nano Energy. **78**, 105251 (2020). https://doi.org/10.1016/j.nanoen.2020.105251

12. W. Zhai, J. Nie, L. Zhu. Enhanced flexible poly(vinylidene fluoride-trifluorethylene) piezoelectric nanogenerators by SnSe nanosheet doping and solvent treatment. ACS Appl Mater Interfaces. **13**(27), 32278-32285 (2021). https://doi.org/10.1021/acsami.1c08347

13. Q. Xu, J. Wen, Y. Qin. Development and outlook of high output piezoelectric

nanogenerators. Nano Energy. **86**, 106080 (2021). https://doi.org/10.1016/j.nanoen.2021.106080

14. S. Ye, C. Cheng, X. Chen, X. Chen, J. Shao, J. Zhang, H. Hu, H. Tian, X. Li, L. Ma, W. Jia. High-performance piezoelectric nanogenerator based on microstructured P(VDF-TrFE)/bnnts composite for energy harvesting and radiation protection in space. Nano Energy. **60**, 701-714 (2019). https://doi.org/10.1016/j.nanoen.2019.03.096

15. J. Yan, M. Liu, Y. G. Jeong, W. Kang, L. Li, Y. Zhao, N. Deng, B. Cheng, G. Yang. Performance enhancements in poly(vinylidene fluoride)-based piezoelectric nanogenerators for efficient energy harvesting. Nano Energy. **56**, 662-692 (2019). https://doi.org/10.1016/j.nanoen.2018.12.010

16. D. Wang, D. Zhang, P. Li, Z. Yang, Q. Mi, L. Yu. Electrospinning of flexible poly(vinyl alcohol)/mxene nanofiber-based humidity sensor self-powered by monolayer molybdenum diselenide piezoelectric nanogenerator. Nanomicro Lett. **13**(1), 57 (2021). https://doi.org/10.1007/s40820-020-00580-5

17. D. Hu, M. Yao, Y. Fan, C. Ma, M. Fan, M. Liu. Strategies to achieve high performance piezoelectric nanogenerators. Nano Energy. **55**, 288-304 (2019). https://doi.org/10.1016/j.nanoen.2018.10.053

18. H. Li, C. R. Bowen, Y. Yang. Scavenging energy sources using ferroelectric materials. Adv Funct Mater. **31**(25), 2100905 (2021). https://doi.org/10.1002/adfm.202100905

19. Z. Zhou, Z. Zhang, Q. Zhang, H. Yang, Y. Zhu, Y. Wang, L. Chen. Controllable core-shell $BaTiO_3$@carbon nanoparticle-enabled P(VDF-TrFE) composites: A cost-

effective approach to high-performance piezoelectric nanogenerators. ACS Appl Mater Interfaces. **12**(1), 1567-1576 (2020). https://doi.org/10.1021/acsami.9b18780

20. K. Shi, B. Chai, H. Zou, P. Shen, B. Sun, P. Jiang, Z. Shi, X. Huang. Interface induced performance enhancement in flexible $BaTiO_3$/PVDF-TrFE based piezoelectric nanogenerators. Nano Energy. **80**, 105515 (2021). https://doi.org/10.1016/j.nanoen.2020.105515

21. B. Liu, B. Lu, X. Chen, X. Wu, S. Shi, L. Xu, Y. Liu, F. Wang, X. Zhao, W. Shi. A high-performance flexible piezoelectric energy harvester based on lead-free $(Na_{0.5}Bi_{0.5})TiO_3$–$BaTiO_3$ piezoelectric nanofibers. J Mater Chem A. **5**(45), 23634-23640 (2017). https://doi.org/10.1039/c7ta07570g

22. H. Luo, X. Zhou, R. Guo, X. Yuan, H. Chen, I. Abrahams, D. Zhang. 3D printing of anisotropic polymer nanocomposites with aligned $BaTiO_3$ nanowires for enhanced energy density. Materials Advances. **1**(1), 14-19 (2020). https://doi.org/10.1039/d0ma00045k

23. Z. Zhou, C. C. Bowland, M. H. Malakooti, H. Tang, H. A. Sodano. Lead-free $0.5Ba(Zr_{0.2}Ti_{0.8})O_3$-$0.5(Ba_{0.7}Ca_{0.3})TiO_3$ nanowires for energy harvesting. Nanoscale. **8**(9), 5098-5105 (2016). https://doi.org/10.1039/c5nr09029f

24. G. Zhang, P. Zhao, X. Zhang, K. Han, T. Zhao, Y. Zhang, C. K. Jeong, S. Jiang, S. Zhang, Q. Wang. Flexible three-dimensional interconnected piezoelectric ceramic foam based composites for highly efficient concurrent mechanical and thermal energy harvesting. Energy Environ Sci. **11**(8), 2046-2056 (2018). https://doi.org/10.1039/c8ee00595h

25. D. Y. Hyeon, K. I. Park. Vertically aligned piezoelectric perovskite nanowire array on flexible conducting substrate for energy harvesting applications. Adv Mater Technol. **4**(8), 1900228 (2019). https://doi.org/10.1002/admt.201900228

26. B. Xie, H. Zhang, Q. Zhang, J. Zang, C. Yang, Q. Wang, M.-Y. Li, S. Jiang. Enhanced energy density of polymer nanocomposites at a low electric field through aligned $BaTiO_3$ nanowires. J Mater Chem A. **5**(13), 6070-6078 (2017). https://doi.org/10.1039/c7ta00513j

27. G. Zhu, A. C. Wang, Y. Liu, Y. Zhou, Z. L. Wang. Functional electrical stimulation by nanogenerator with 58 V output voltage. Nano Lett. **12**(6), 3086-3090 (2012). https://doi.org/10.1021/nl300972f

28. M. H. Malakooti, F. Julé, H. A. Sodano. Printed nanocomposite energy harvesters with controlled alignment of barium titanate nanowires. ACS Appl Mater Interfaces. **10**(44), 38359-38367 (2018). https://doi.org/10.1021/acsami.8b13643

29. Z. Wang, Y. Zhang, S. Yang, Y. Hu, S. Wang, H. Gu, Y. Wang, H. L. Chan, J. Wang. $(K,Na)NbO_3$ nanofiber-based self-powered sensors for accurate detection of dynamic strain. ACS Appl Mater Interfaces. **7**(8), 4921-4927 (2015). https://doi.org/10.1021/am5090012

30. J. Fu, Y. Hou, X. Gao, M. Zheng, M. Zhu. Highly durable piezoelectric energy harvester based on a pvdf flexible nanocomposite filled with oriented $BaTi_2O_5$ nanorods with high power density. Nano Energy. **52**, 391-401 (2018). https://doi.org/10.1016/j.nanoen.2018.08.006

31. X. Gao, M. Zheng, X. Yan, J. Fu, M. Zhu, Y. Hou. The alignment of BCZT particles

in pdms boosts the sensitivity and cycling reliability of a flexible piezoelectric touch sensor. J Mater Chem C. **7**(4), 961-967 (2019). https://doi.org/10.1039/C8TC04741C

32. H. Tang, Y. Lin, H. A. Sodano. Enhanced energy storage in nanocomposite capacitors through aligned PZT nanowires by uniaxial strain assembly. Adv Energy Mater. **2**(4), 469-476 (2012). https://doi.org/10.1002/aenm.201100543

33. D. Yao, H. Cui, R. Hensleigh, P. Smith, S. Alford, D. Bernero, S. Bush, K. Mann, H. F. Wu, M. Chin-Nieh, G. Youmans, X. Zheng. Achieving the upper bound of piezoelectric response in tunable, wearable 3D printed nanocomposites. Adv Funct Mater. **29**(42), 1903866 (2019). https://doi.org/10.1002/adfm.201903866

34. S. Safaee, M. Schock, E. B. Joyee, Y. Pan, R. K. Chen. Field-assisted additive manufacturing of polymeric composites. Additive Manufacturing. **51**, 102642 (2022). https://doi.org/10.1016/j.addma.2022.102642

35. J. Fan, N. Deneke, S. Xu, B. Newell, J. Garcia, C. Davis, W. Wu, R. M. Voyles, R. A. Nawrocki. Electric poling-assisted additive manufacturing technique for piezoelectric active poly(vinylidene fluoride) films: Towards fully three-dimensional printed functional materials. Additive Manufacturing. **60**, 103248 (2022). https://doi.org/10.1016/j.addma.2022.103248

36. J. Chen, X. Liu, Y. Tian, W. Zhu, C. Yan, Y. Shi, L. B. Kong, H. J. Qi, K. Zhou. 3D-printed anisotropic polymer materials for functional applications. Adv Mater. **34**(5), e2102877 (2022). https://doi.org/10.1002/adma.202102877

37. Z. Guo, C. Zhou. Recent advances in ink-based additive manufacturing for porous structures. Additive Manufacturing. **48**, 102405 (2021).

https://doi.org/10.1016/j.addma.2021.102405

38. M. Gao, L. Li, W. Li, H. Zhou, Y. Song. Direct writing of patterned, lead-free nanowire aligned flexible piezoelectric device. Adv Sci (Weinh). **3**(8), 1600120 (2016). https://doi.org/10.1002/advs.201600120

39. Y. Wu, F. Ma, J. Qu, Y. Luo, C. Lv, Q. Guo, T. Qi. Vertically-aligned lead-free BCZTY nanofibers with enhanced electrical properties for flexible piezoelectric nanogenerators. Appl Surf Sci. **469**, 283-291 (2019). https://doi.org/10.1016/j.apsusc.2018.10.229

40. M. J. Bauer, C. S. Snyder, C. C. Bowland, A. M. Uhl, M. A. K. Budi, M. Villancio-Wolter, H. A. Sodano, J. S. Andrew. Structure-property relationships in aligned electrospun barium titanate nanofibers. J Am Ceram Soc. **99**(12), 3902-3908 (2016). https://doi.org/10.1111/jace.14455

41. C. C. Jin, X. C. Liu, C. H. Liu, Y. Wang, H. L. Hwang, Q. Wang. High-performance bctz nanowires-based energy harvesting device and self-powered bio-compatible flexion sensor. Mater Des. **144**, 55-63 (2018). https://doi.org/10.1016/j.matdes.2018.02.008

42. Y. Zhang, C. K. Jeong, T. Yang, H. Sun, L.-Q. Chen, S. Zhang, W. Chen, Q. Wang. Bioinspired elastic piezoelectric composites for high-performance mechanical energy harvesting. J Mater Chem A. **6**(30), 14546-14552 (2018). https://doi.org/10.1039/c8ta03617a

43. Y. Zhang, L. Zhou, X. Gao, C. Liu, H. Chen, H. Zheng, J. Gui, C. Sun, L. Yu, S. Guo. Performance-enhanced flexible piezoelectric nanogenerator via layer-by-layer

assembly for self-powered vagal neuromodulation. Nano Energy. **89**, 106319 (2021). https://doi.org/10.1016/j.nanoen.2021.106319

44. J. Fu, Y. Hou, M. Zheng, Q. Wei, M. Zhu, H. Yan. Improving dielectric properties of PVDFcomposites by employing surface modified strong polarized $BaTiO_3$ particles derived by molten salt method. ACS Appl Mater Interfaces. **7**(44), 24480-24491 (2015). https://doi.org/10.1021/acsami.5b05344

45. Q. Wu, H. Guo, H. Sun, X. Liu, H. Sui, F. Wang. Flexible piezoelectric energy harvesters with graphene oxide nanosheets and pzt-incorporated P(VDF-TrFE) matrix for mechanical energy harvesting. Ceram Int. **47**(14), 19614-19621 (2021). https://doi.org/10.1016/j.ceramint.2021.03.299

46. J. Kim, J.-H. Ji, D.-J. Shin, S. Yoon, Y.-H. Ko, K.-H. Cho, J.-H. Koh. 2-dimensional rGO introduced PMN-PT and P(VDF-TrFE) flexible films for enhanced piezoelectric energy harvester. Appl Surf Sci. **494**, 1000-1006 (2019). https://doi.org/10.1016/j.apsusc.2019.06.236

47. X. Zhou, K. Parida, O. Halevi, Y. Liu, J. Xiong, S. Magdassi, P. S. Lee. All 3D-printed stretchable piezoelectric nanogenerator with non-protruding kirigami structure. Nano Energy. **72**, 104676 (2020). https://doi.org/10.1016/j.nanoen.2020.104676

48. R. Guo, H. Luo, M. Yan, X. Zhou, K. Zhou, D. Zhang. Significantly enhanced breakdown strength and energy density in sandwich-structured nanocomposites with low-level $BaTiO_3$ nanowires. Nano Energy. **79**, 105412 (2021). https://doi.org/10.1016/j.nanoen.2020.105412

49. H. Lu, J. Zhang, L. Yang, Y. Zhang, Y. Wu, H. Zheng. Enhanced output performance

of piezoelectric nanogenerators by Tb-modified (BaCa)(ZrTi)O_3 and 3D core/shell structure design with pvdf composite spinning for microenergy harvesting. ACS Appl Mater Interfaces. **14**(10), 12243-12256 (2022). https://doi.org/10.1021/acsami.1c23946